Near-infrared light curves of Type Ia supernovae: studying properties of the second maximum

S. Dhawan,[1,2,3]★ B. Leibundgut,[1,2] J. Spyromilio[1] and K. Maguire[1]

[1]*European Southern Observatory, Karl-Schwarzschild-Strasse, 2, D-85748 Garching bei München, Germany*
[2]*Excellence Cluster Universe, Technische Universität München, Boltzmannstrasse 2, D-85748 Garching, Germany*
[3]*Physik Department, Technische Universität München, James-Franck-Strasse 1, D-85748 Garching bei München, Germany*

ABSTRACT

Type Ia supernovae (SNe Ia) have been proposed to be much better distance indicators at near-infrared (NIR) compared to optical wavelengths – the effect of dust extinction is expected to be lower and it has been shown that SNe Ia behave more like 'standard candles' at NIR wavelengths. To better understand the physical processes behind this increased uniformity, we have studied the *Y, J* and *H*-filter light curves of 91 SNe Ia from the literature. We show that the phases and luminosities of the first maximum in the NIR light curves are extremely uniform for our sample. The phase of the second maximum, the late-phase NIR luminosity and the optical light-curve shape are found to be strongly correlated, in particular more luminous SNe Ia reach the second maximum in the NIR filters at a later phase compared to fainter objects. We also find a strong correlation between the phase of the second maximum and the epoch at which the SN enters the Lira law phase in its optical colour curve (epochs $\sim$ 15 to 30 d after *B*-band maximum). The decline rate after the second maximum is very uniform in all NIR filters. We suggest that these observational parameters are linked to the nickel and iron mass in the explosion, providing evidence that the amount of nickel synthesized in the explosion is the dominating factor shaping the optical and NIR appearance of SNe Ia.

Key words: supernovae: general – distance scale.

1 INTRODUCTION

The uniformity of Type Ia supernovae (SNe Ia) has led to their use, after calibration, as distance indicators (reviewed in Goobar & Leibundgut 2011) and they provided the first evidence for the accelerated expansion of the Universe (Riess et al. 1998; Perlmutter et al. 1999).

Observations of large SN Ia samples show that the peak luminosity in the optical is not uniform but can be normalized following a variety of calibration techniques, most notably the correlation between light-curve shape and peak luminosity, and between light-curve colour and peak luminosity (e.g. Phillips 1993; Riess, Press & Kirshner 1996; Guy et al. 2005, 2007, 2010; Jha, Riess & Kirshner 2007). The variation in bolometric luminosity for the objects (Contardo, Leibundgut & Vacca 2000) implies variations in the physical parameters of the explosion, in particular the synthesized Ni mass and the total ejected mass (Stritzinger et al. 2006; Scalzo et al. 2014).

At near-infrared (NIR) wavelengths (900 > λ > 2000 nm), SNe Ia have a very uniform brightness distribution without any prior normalization (Elias et al. 1981; Meikle 2000; Krisciunas et al. 2004a, 2007). The scatter in the peak luminosity in these studies is $\sim$0.2 mag, which when combined with the lower sensitivity of the NIR to extinction by dust, has sparked interest in the use of this wavelength region. Following large observational campaigns, statistically significant samples of SN Ia light curves have been made public (Wood-Vasey et al. 2008; Contreras et al. 2010; Stritzinger et al. 2011; Barone-Nugent et al. 2012), and have been used to construct the first rest-frame NIR Hubble diagrams (Nobili et al. 2005; Freedman et al. 2009; Kattner et al. 2012; Weyant et al. 2014).

Dust extinction in the NIR is significantly reduced compared to the optical leading to smaller corrections and uncertainties. In addition to the photometric calibration systematics (see Conley et al. 2011), the dust extinction for SNe Ia is one of the major sources of systematics in SN Ia cosmology measurements (e.g. Peacock et al. 2006; Goobar & Leibundgut 2011). In particular, extinction law measurements for galaxies remains uncertain (see discussions in Phillips et al. 2013; Scolnic et al. 2014). The recent SN 2014J is a case in point with derived dust properties very different from local interstellar dust (Amanullah et al. 2014; Foley et al. 2014). Strongly

reddened SNe Ia may also exhibit variations in their light-curve shapes (Leibundgut 1988; Amanullah et al. 2014).

The light-curve morphology in the NIR is markedly different from that in the optical with a pronounced second maximum in *IYJHK* filters for 'normal' SNe Ia (Elias et al. 1981, 1985; Leibundgut 1988, 2000; Meikle 2000; Wood-Vasey et al. 2008; Folatelli et al. 2010). The formation of the NIR spectrum in SNe Ia is highly sensitive to the opacity variations (Spyromilio, Pinto & Eastman 1994; Wheeler et al. 1998) as the spectrum is dominated by line blanketing opacity making the evolution of the NIR light a sensitive probe of the structure of the ejecta. Kasen (2006) in a detailed study suggested that the second maximum is a result of a decrease in opacity due to the ionization change of Fe-group elements from doubly to singly ionized atoms, which preferentially radiate the energy at NIR wavelengths. A direct prediction of Kasen (2006) is that a larger iron mass leads to a later NIR second maximum.

Studies of the *i*-band light curve find a relation between the phase of the second maximum and the optical light-curve shape (e.g. $\Delta m_{15}(B)$; Hamuy et al. 1996; Folatelli et al. 2010). The strength of the second maximum in *i* does not show such a correlation.

In this paper, we investigate the properties of SN Ia NIR light curves (*YJH*) and establish correlations with other observational characteristics. Connections to possible physical properties in the explosions are explored. The structure of this paper is as follows: after a presentation of the input data in Section 2, we analyse the NIR light-curve properties (Section 3) along with a description of NIR colours. Correlations with optical light-curve parameters and their interpretations are given in Section 4 followed by a discussion in Section 5. The conclusions are presented in Section 6.

2 DATA

We investigate a large sample of nearby objects with well-sampled optical and NIR data (Table 1). The main data source of NIR SN Ia photometry is the Carnegie SN Project (CSP; Contreras et al. 2010; Burns et al. 2011, 2014; Stritzinger et al. 2011; Phillips 2012). The low-redshift CSP provides a sample of SNe Ia with optical and NIR light curves in a homogeneous and well-defined photometric system (in Vega magnitude system) and thus forms an ideal basis for the evaluation of light-curve properties. CSP relies primarily on SN discoveries from the Lick Observatory SN Search (Leaman et al. 2011). The CSP has published light curves on a total of 82 SNe Ia of which 70 have photometry in *YJHK* bands.

From the CSP NIR data set, we removed spectroscopically peculiar objects such as SN2006bt and SN2006ot. We also rejected SNe Ia with spectra similar to the peculiar SN 1991bg (Filippenko et al. 1992; Leibundgut et al. 1993; Mazzali et al. 1997) and objects that do not exhibit a second maximum (SNe 2005bl, 2005ke, 2005ku, 2006bd, 2006mr, 2007N, 2007ax, 2007ba, 2009F).

We have included in our sample NIR SN Ia photometry from Meikle (2000) and several SNe Ia observed by the European SN Consortium (ESC; Benetti et al. 2004; Elias-Rosa et al. 2006; Pastorello et al. 2007; Pignata et al. 2008; Krisciunas et al. 2009). Twelve SNe Ia have been discussed by Barone-Nugent et al. (2012) and have data only near the first maximum. We also included NIR photometry from two recent nearby explosions, SN2011fe (Matheson et al. 2012) and SN2014J (Foley et al. 2014).

The 91 objects used in this work are listed in Table 1, where the phase range of observations (first and last observation), total number of observations in each filter and the reference for each data set are tabulated. The sample is dominated by SNe Ia from the CSP and we show the results separately for the CSP and non-CSP objects.

Table 1. SN sample.

SN name	Phase range (d)			N_i	N_Y	N_J	N_H	N_K	Reference
SN1980N	5.7	...	99.7	–	–	11	13	–	M00
SN1981B	2.7	...	120.5	–	–	17	17	–	M00
SN1986G	−6.1	to	101.0	–	–	28	29	–	M00
SN1998bu	−8.5	to	31.5	–	–	23	23	–	M00
SN1999ac	−13.1	to	63.8	–	–	30	30	–	Ph06
SN1999ee	−7.5	to	27.5	–	17	18	20	–	K04a
SN1999ek	−8.0	to	23.0	–	–	14	15	–	K04a
SN2000E	−7.7	to	126.6	–	–	18	18	–	V03
SN2000bh	−5.5	to	39.0	–	6	21	22	–	K04a
SN2001ba	−6.0	to	34.9	–	–	14	15	–	K04a
SN2001bt	−1.6	to	65.3	–	–	21	21	–	K04a
SN2001cn	4.2	...	59.1	–	–	19	19	–	K04b
SN2001cz	−2.4	to	47.6	–	–	12	12	–	K04b
SN2001el	−10.6	to	64.3	–	–	33	32	–	K03
SN2002bo	−11.0	to	44.0	–	–	17	17	17	K04b, ESC
SN2002dj	−11.0	to	67.0	–	–	21	21	–	P08, ESC
SN2002fk	−12.2	to	102.1	–	–	24	23	23	C13
SN2003cg	−6.4	to	413.5	–	–	13	13	–	ER06, ESC
SN2003hv	1.2	...	62.0	–	16	16	16	–	L09, ESC
SN2004ef	−8.7	to	65.2	46	4	3	4	3	CSP
SN2004eo	−12.0	to	63.0	39	8	9	9	8	CSP, P07, ESC
SN2004ey	−8.9	to	48.1	32	7	9	9	8	CSP
SN2004gs	−3.6	to	99.1	50	12	11	10	–	CSP
SN2004gu	−0.4	to	48.6	27	8	7	7	–	CSP
SN2005A	−3.5	to	30.4	35	10	10	10	–	CSP
SN2005M	−8.0	to	74.7	56	17	17	14	12	CSP
SN2005ag	−1.7	to	66.3	44	9	9	9	–	CSP
SN2005al	−1.0	to	82.0	35	7	8	8	7	CSP
SN2005am	−4.6	to	75.3	36	6	6	6	6	CSP
SN2005el	−7.3	to	83.6	25	21	22	15	3	CSP
SN2005eq	−3.6	to	97.3	27	15	15	10	1	CSP
SN2005hc	−4.5	to	84.4	22	13	11	9	–	CSP
SN2005hj	−2.3	to	87.6	16	11	12	10	1	CSP
SN2005iq	−5.3	to	67.7	19	11	11	11	1	CSP
SN2005kc	−10.4	to	30.6	13	9	9	8	–	CSP
SN2005ki	−9.9	to	155.8	47	12	11	10	–	CSP
SN2005na	−1.8	to	94.0	27	14	11	12	–	CSP
SN2006D	−6.0	to	112.8	42	17	16	16	6	CSP
SN2006X	−11.0	to	119.8	39	32	33	32	9	CSP, ESC
SN2006ax	−11.7	to	71.2	26	19	18	16	3	CSP
SN2006bh	−4.9	to	60.0	24	12	11	10	–	CSP
SN2006br	5.8	...	37.7	9	5	5	5	–	CSP
SN2006ej	4.4	...	69.4	13	3	3	3	–	CSP
SN2006eq	0.2	to	43.0	18	10	7	8	–	CSP
SN2006et	−7.2	to	105.7	23	18	12	13	–	CSP
SN2006ev	4.2	...	48.1	12	10	8	8	–	CSP
SN2006gj	−1.8	to	96.0	19	13	10	4	–	CSP
SN2006gt	−2.1	to	62.8	13	10	8	6	–	CSP
SN2006hb	7.2	...	136.9	25	10	10	9	–	CSP
SN2006hx	−9.3	to	30.7	8	7	6	5	–	CSP
SN2006is	6.4	...	118.2	24	8	8	7	–	CSP
SN2006kf	−4.8	to	86.0	20	17	14	11	3	CSP
SN2006lu	5.1	...	90.1	21	6	4	3	–	CSP
SN2006ob	−2.6	to	58.3	13	12	9	5	–	CSP
SN2006os	2.4	...	57.3	14	10	6	5	–	CSP
SN2007A	−4.7	to	18.3	9	9	5	3	–	CSP
SN2007S	−10.5	to	102.2	19	12	17	18	7	CSP
SN2007af	−8.8	to	82.1	28	26	25	24	5	CSP
SN2007ai	−0.4	to	86.4	17	7	7	6	3	CSP
SN2007as	−0.0	to	77.7	19	11	10	10	–	CSP
SN2007bc	−3.0	to	58.8	10	11	8	6	–	CSP
SN2007bd	−9.5	to	215.8	14	12	9	7	–	CSP
SN2007bm	−0.2	to	34.7	10	10	9	7	–	CSP

Table 1 – *continued*

SN name	Phase range (d)			N_i	N_Y	N_J	N_H	N_K	Reference
SN2007ca	-8.8	to	32.1	12	10	8	7	2	CSP
SN2007if	14.4	...	100.2	16	8	7	5	–	CSP
SN2007jg	-3.1	to	58.8	18	8	6	5	–	CSP
SN2007le	-11.5	to	71.2	26	17	17	16	–	CSP
SN2007nq	-1.4	to	77.5	25	19	10	4	...	CSP
SN2007on	-8.6	to	88.2	38	29	28	25	7	CSP
SN2008C	2.9	...	85.6	19	15	13	18	1	CSP
SN2008R	-1.3	to	32.6	12	8	7	5	–	CSP
SN2008bc	-9.3	to	96.6	32	7	12	11	–	CSP
SN2008bq	-0.8	to	43.1	16	4	4	4	–	CSP
SN2008fp	-6.0	...	89.9	28	22	20	20	7	CSP
SN2008gp	-10.5	to	34.4	19	10	11	9	–	CSP
SN2008hv	-10.5	to	78.3	25	18	16	16	–	CSP
SN2008ia	-3.5	to	43.5	15	16	15	14	–	CSP
PTF09dlc	-5.56	to	19.5	–	–	4	4	–	BN12
PTF10hdv	-3.9	to	10.3	–	–	4	4	–	BN12
PTF10hmv	-10.1	to	7.9	–	–	–	5	–	BN12
PTF10mwb	-12.3	to	5.7	–	–	5	5	–	BN12
PTF10ndc	-3.9	to	5.1	–	–	4	4	–	BN12
PTF10nlg	-5.1	to	3.9	–	–	3	5	–	BN12
PTF10qyx	-3.5	to	7.5	–	–	4	4	–	BN12
PTF10tce	-6.6	to	6.5	–	–	4	4	–	BN12
PTF10ufj	-9.0	to	4.1	–	–	4	4	–	BN12
PTF10wnm	-7.1	to	4.8	–	–	4	4	–	BN12
PTF10wof	-3.9	to	9.1	–	–	4	4	–	BN12
PTF10xyt	-4.6	to	7.3	–	–	2	5	–	BN12
SN2011fe	-16.0	to	45.9	–	–	32	35	32	M12
SN2014J	-10.0	to	72.4	–	–	24	24	24	F14

References: M00 – Meikle (2000); Ph06 – Phillips et al. (2006); K04a – Krisciunas et al. (2004a); V03 – Valentini et al. (2003); K04b – Krisciunas et al. (2004b); K03 – Krisciunas et al. (2003); P08 – Pignata et al. (2008); C13 – Cartier et al. (2014); ER06 – Elias-Rosa et al. (2006); L09 – Leloudas et al. (2009); P07 – Pastorello et al. (2007); CSP – Carnegie Supernova Project Contreras et al. (2010); Stritzinger et al. (2011); BN12 – Barone-Nugent et al. (2012); M12 – Matheson et al. (2012); F14 – Foley et al. (2014).

It is worth noting that there are 15 SNe Ia with observed NIR light curves beyond 100 d.

As can be seen in Table 1 and displayed in Fig. 1, the *K*-band light curves are sparsely sampled and not enough objects are available for detailed analysis. Therefore, we exclude the *K*-band light curves from further analysis.

3 NIR LIGHT-CURVE MORPHOLOGY

In parameterizing the NIR light curves, we follow the nomenclature introduced by Biscardi et al. (2012). The first maximum in filter X, $M_1(X)$ is reached at a phase, $t_1(X)$ relative to the phase of the B maximum ($t_B^{\max} = 0$ d). The light curves dip to a minimum $M_0(X)$ at $t_0(X)$ before reaching a second maximum, $M_2(X)$ at time, $t_2(X)$. These three prominent features are shown in Fig. 1. The light curves are plotted without normalization for phase or corrections for possible differences in photometric systems or absorption.

3.1 Light-curve fitting

We fit the optical light curves using the programme SNooPy (Burns et al. 2011) to determine the peak of the *B*-band light curve through cubic-spline fitting and determine the phase, $t_B^{\max}$ used throughout this work and the peak brightness $m_B^{\max}$. SNooPY also determines the Δm_{15} parameter[1] commonly used to characterize the SN light-curve shape and provides an estimate of the extinction in the host galaxy. The SNooPy light-curve-fitting parameters and distance moduli for the SNe Ia in our sample are given in Table 2. We used the published values of the distance modulus, μ, for non-CSP objects, (references in Table 2). The distance moduli for CSP SNe Ia not in the Hubble flow are taken from Contreras et al. (2010) and Stritzinger et al. (2011), and the individual references are listed in Table 2. The distance moduli for the rest of the SNe are based on the host galaxy redshift from the NASA/IPAC Extragalactic Database adopting a Hubble constant of $H_0 = 70$ km s^{-1} Mpc^{-1}.

While the extinction is much reduced in the NIR, it is not entirely negligible. Using the Cardelli extinction law (Cardelli, Clayton & Mathis 1989), the extinction in the *H* band is ∼18 per cent of that in the *V* band. We have also included some heavily extinguished SNe Ia like SNe 1986G, 2005A, 2006X, 2006br and 2014J without an extinction correction in our sample. Therefore, the observed scatter is larger than the intrinsic variation among SNe Ia. We have chosen not to apply a correction for the host galaxy extinction as the reddening law remains under debate (e.g. Phillips et al. 2013).

We fit a spline interpolation to the data to derive the phase and magnitude at maximum, the minimum and the second maximum in each filter. In order for a measurement of the minimum and second maximum to be made, we require ≥4 observations at late phases (>7 d for the minimum and >15 d for the second maximum). We also require that observations at least 4 d before $t_{\max}$ were available. The uncertainties for each derived parameter were calculated by repeating the fits to 1000 Monte Carlo realizations of light curves generated using the errors on the photometry.

The NIR light curves are very uniform up to the time of the *B*-band maximum, ∼3–4 d after the maximum is reached in the NIR light curves. In the lower panels in Fig. 1, we show the rms scatter for each epoch.

The scatter remains small for ∼1 week around maximum in the different bands independent of the sample (CSP or non-CSP). The two samples show very consistent scatter out to a phase of ∼10 d in *J* and ∼25 d in *H*, after which they start to deviate. With only 14 objects in the non-CSP sample in this phase range compared to 25 from the CSP, we consider the differences not statistically significant. The scatter continues to increase beyond 35 d, which we attribute to the colour evolution (see Section 3.6 below).

3.2 The first maximum

Elias et al. (1981) showed, in a small sample of SNe Ia, that the *JHK* light curves of SNe Ia peak earlier than the optical light curves. We confirm this for our sample (Fig. 2).

The NIR light curves peak within -2 to -7 d of the *B*-band peak confirming the result of Folatelli et al. (2010) for SNe Ia with $\Delta m_{15}(B) < 1.8$. There is no obvious difference between our full sample and the CSP sample as seen in the scatter. The distribution of t_1 is remarkably tight (less than 1 d dispersion) for all filters. This indicates a close relationship between $t_B^{\max}$ and the NIR t_1 values for the SNe Ia in our sample.

Table 3 gives the phase of lowest scatter measured in each filter. Without any attempt to normalize the light curves, we find the

---

[1] The Δm_{15} is calculated by SNooPy from all available filters. It is linearly related to $\Delta m_{15}(B)$ (see Burns et al. 2011).
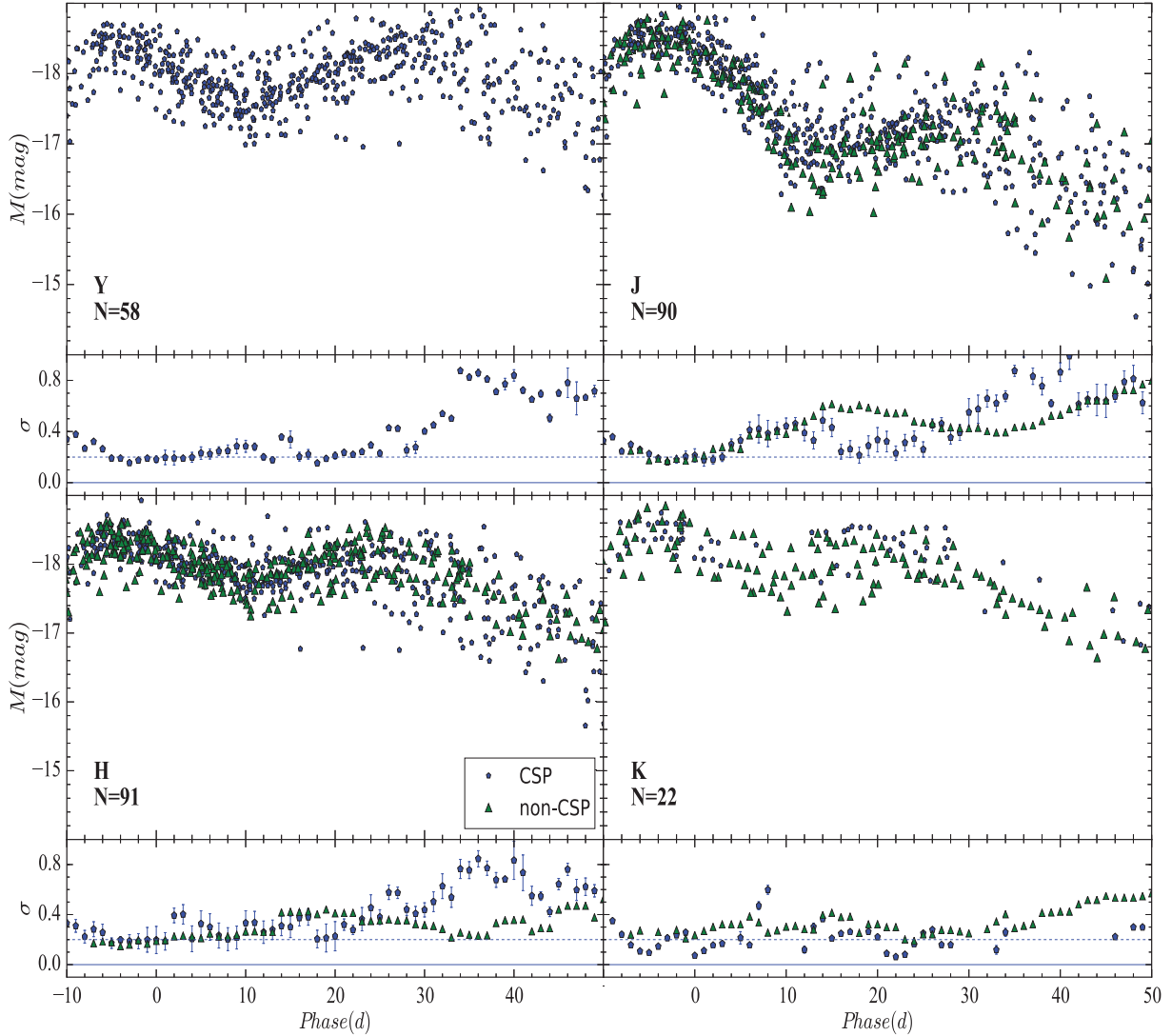
Figure 1. The *Y, J, H* and *K* absolute magnitude light curves of SNe Ia. The CSP sample is shown as blue pentagons. The green triangles indicate the non-CSP sample (see Table 1 for the references). The root-mean-square (rms) scatter for each day is shown in the lower panels. For guidance, a line at a scatter of 0.2 mag is drawn in each panel. The luminosities are based on the literature distances (cf. Table 2) and no correction has been applied. The steady increase of the scatter after the first maximum is evident.

smallest scatter in all NIR light curves near t_1. The dispersion remains very low for ∼1 week, before increasing to >0.2 mag at later phases.

3.3 The minimum

The minimum in *J* occurs ∼2 weeks after t_B^{max} (Fig. 3). The *Y* light curves dip about 3 d earlier at $t_0 = +11$ d. The minimum in *H* is reached on average about 2 d before *J* at $t_0 = +12$ d. The phase range is still relatively narrow with the minima all occurring within roughly ±2 d. While *Y* and *H* display a tight distribution of t_0, the *J* distribution exhibits a tail of late minima.

No significant difference between the CSP and the literature samples can be seen in the distributions. The scatter among M_0 is fairly small for the three NIR bands although about two to three times larger than at t_1. In the *Y* band, the scatter is low (<0.2 mag) immediately after t_0, while the *J* and *H* light curves display a larger dispersion at this point.

3.4 The second maximum

Fig. 4 shows that t_2 occurs over a wide range of phases and can vary by as much as 20 d from one SN Ia to another. This diversity had been observed before for the *i* light curves (e.g. Hamuy et al. 1996; Folatelli et al. 2010) and for *JHK* (Mandel et al. 2009; Biscardi et al. 2012). In Fig. 4, we show that the mean t_2 is later in the *Y* and *J* bands, with the *H*-band light curves reaching t_2, on average, a few days earlier. The scatter in the luminosity starts to increase slowly after t_0, and is seen to increase significantly (>0.5 mag) around the time of t_2 (Fig. 1).

3.5 The late decline

After the second maximum, the light curves steadily decline. In Fig. 5, we show the distribution of slopes calculated for SNe Ia with at least three observations in phases $40 < t < 90$ d. This choice of phase range ensures that the measurements are not influenced by

Table 2. Timing of B_{max}, Δm_{15}, distance modulus for the SN in our sample. References for the published distance moduli are provided in the footnote.

SN Name	$t(B_{max})$ (MJD)	err	Δm_{15} (mag)	err	μ (mag)	err
SN1980N	44 585.8	0.5	1.28	0.04	31.59	0.10
SN1981B	44 672.0	0.2	1.10	0.04	30.95	0.07
SN1986G	46 561.0	0.1	1.76	0.10	28.01	0.12
SN1998bu	50 953.3	0.5	1.01	0.02	30.20	0.10
SN1999ac	51 251.0	0.5	1.34	0.02	33.50	0.30
SN1999ee	51 469.1	0.5	1.09	0.02	33.20	0.20
SN1999ek	51 481.8	0.1	1.17	0.03	34.40	0.30
SN2000E	51 557.0	0.5	0.99	0.02	31.90	0.40
SN2000bh	51 635.2	0.5	1.16	0.01	34.60	0.30
SN2001ba	52 034.5	0.5	0.97	0.05	35.40	0.50
SN2001bt	52 063.4	0.5	1.18	0.02	34.10	0.40
SN2001cn	52 071.6	0.2	1.15	0.02	34.10	0.30
SN2001cz	52 103.9	0.1	1.05	0.07	33.50	0.10
SN2001el	52 182.5	0.5	1.13	0.04	31.30	0.20
SN2002bo	52 356.5	0.2	1.12	0.02	31.80	0.20
SN2002dj	52 450.0	0.7	1.08	0.02	32.90	0.30
SN2002fk	52 547.9	0.3	1.02	0.04	32.59	0.15
SN2003cg	52 729.4	0.5	1.12	0.04	31.28	0.20
SN2003hv	52 891.2	0.3	1.09	0.02	31.40	0.30
SN2004ef	53 264.4	0.1	1.45	0.01	35.57	0.07
SN2004eo	53 278.4	0.1	1.32	0.01	34.03	0.10
SN2004ey	53 304.3	0.1	1.02	0.01	34.01	0.12
SN2004gs	53 356.2	0.1	1.53	0.01	35.40	0.08
SN2004gu	53 362.2	0.2	0.80	0.01	36.59	0.04
SN2005A	53 379.7	0.2	1.08	0.02	34.51	0.11
SN2005M	53 405.4	0.1	0.80	0.04	35.01	0.09
SN2005ag	53 413.7	0.2	0.87	0.01	37.80	0.03
SN2005al	53 430.5	0.1	1.30	0.01	33.79	0.15
SN2005am	53 436.9	0.1	1.48	0.01	32.85	0.20
SN2005el	53 647.0	0.1	1.40	0.01	34.04	0.14
SN2005eq	53 654.4	0.1	0.82	0.01	35.46	0.07
SN2005hc	53 666.7	0.1	0.80	0.01	36.50	0.05
SN2005hj	53 673.8	0.2	0.80	0.02	37.03	0.04
SN2005iq	53 687.7	0.1	1.28	0.01	35.80	0.15
SN2005kc	53 697.7	0.1	1.12	0.02	33.89	0.15
SN2005ki	53 705.5	0.1	1.36	0.01	34.73	0.10
SN2005na	53 740.2	0.1	1.03	0.01	35.34	0.08
SN2006D	53 757.7	0.1	1.47	0.01	33.00	0.15
SN2006X	53 786.3	0.1	1.09	0.03	30.91	0.08
SN2006ax	53 827.2	0.1	1.04	0.01	34.46	0.11
SN2006bh	53 833.6	0.1	1.42	0.01	33.28	0.20
SN2006br	53 853.7	0.6	1.45	0.05	35.23	0.08
SN2006ej	53 976.4	0.2	1.37	0.01	34.62	0.11
SN2006eq	53 975.9	0.4	1.88	0.04	36.66	0.04
SN2006et	53 993.7	0.1	0.88	0.01	34.82	0.10
SN2006ev	53 990.1	0.3	1.34	0.01	35.40	0.08
SN2006gj	54 000.3	0.2	1.56	0.04	35.42	0.08
SN2006gt	54 003.1	0.3	1.71	0.03	36.43	0.05
SN2006hb	54 006.0	0.3	1.69	0.02	34.11	0.13
SN2006hx	54 021.9	0.2	1.07	0.05	36.47	0.05
SN2006is	54 007.5	0.4	0.80	0.01	35.69	0.07
SN2006kf	54 041.3	0.1	1.51	0.01	34.78	0.10
SN2006lu	54 034.4	0.2	0.92	0.01	36.92	0.04
SN2006ob	54 063.4	0.1	1.51	0.01	37.08	0.04
SN2006os	54 063.9	0.2	1.08	0.02	35.70	0.07
SN2007A	54 113.1	0.2	1.06	0.04	34.26	0.13
SN2007S	54 143.8	0.1	0.81	0.01	34.06	0.14
SN2007af	54 174.4	0.1	1.11	0.01	32.10	0.10
SN2007ai	54 173.5	0.3	0.84	0.02	35.73	0.07
SN2007as	54 181.3	0.4	1.27	0.03	34.45	0.12
SN2007bc	54 200.3	0.2	1.27	0.02	34.89	0.10

Table 2 – *continued*

| SN Name	$t(B_{max})$ (MJD)	err	Δm_{15} (mag)	err	μ (mag)	err
SN2007bd	54 206.9	0.1	1.27	0.01	35.73	0.07
SN2007bm	54 224.1	0.2	1.11	0.02	32.30	0.07
SN2007ca	54 227.7	0.2	1.05	0.03	34.04	0.14
SN2007if	54 343.1	0.6	1.07	0.03	37.59	0.03
SN2007jg	54 366.1	0.3	1.09	0.04	36.03	0.06
SN2007le	54 399.3	0.1	1.03	0.02	32.34	0.08
SN2007nq	54 398.8	0.1	1.49	0.01	36.44	0.05
SN2007on	54 419.8	0.4	1.65	0.04	31.45	0.08
SN2008C	54 466.1	0.2	1.08	0.02	34.34	0.12
SN2008R	54 494.5	0.1	1.77	0.04	33.73	0.16
SN2008bc	54 550.0	0.1	1.04	0.02	34.16	0.13
SN2008bq	54 562.1	0.2	0.78	0.02	35.79	0.06
SN2008fp	54 730.9	0.1	1.05	0.01	31.79	0.05
SN2008gp	54 779.1	0.1	1.01	0.01	35.79	0.06
SN2008hv	54 817.1	0.1	1.30	0.01	33.84	0.15
SN2008ia	54 813.2	0.1	1.34	0.01	34.96	0.09
SN2011fe	55 815.0	0.3	1.20	0.02	28.91	0.20
SN2014J	56 689.7	0.3	1.10	0.02	27.64	0.10

References: SN1980N, SN1981B, SN1986G, SN1998bu (Meikle 2000); SN1999ac, SN1999ee, SN2002dj (Willick et al. 1997); SN2000E, SN2002bo (Tully 1988); SN2001el (Ajhar et al. 2001); SN2003hv, SN2007on (Tonry et al. 2001); 2006X (Freedman et al. 2001) (note: we add the correction to μ's from Tonry et al. 2001 and Ajhar et al. 2001 using the values provided in Jensen et al. 2003)
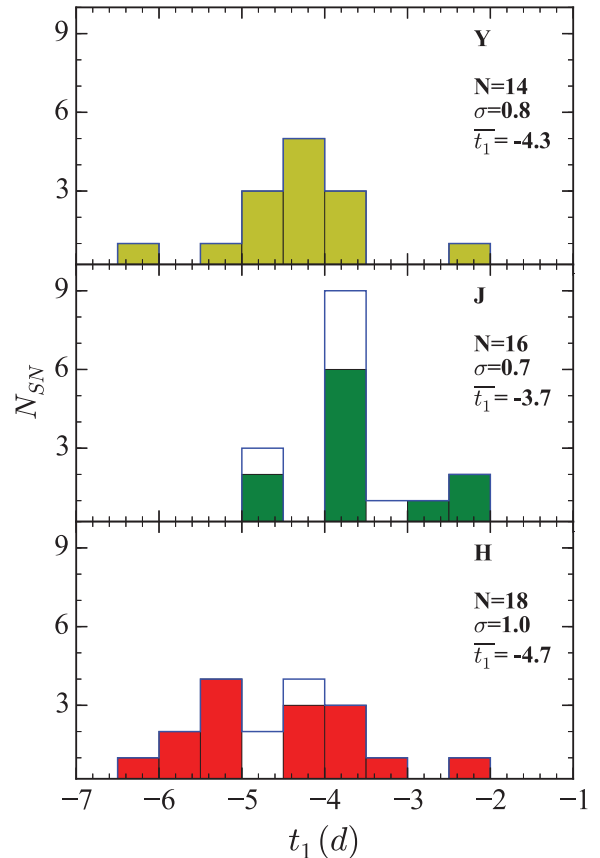
Figure 2. Distribution of t_1 for the Y, J and H light curves relative to the B-band maximum. The filled histograms are for SNe Ia from the CSP sample while the open histograms show the combined CSP and non-CSP sample. In the Y band, we only use the objects observed by the CSP. The NIR light curves peak at within -2 to -7 d relative to the B maximum.

Table 3. Magnitude scatter in NIR light curves. The second column indicates the time of minimum magnitude scatter in each filter, while the third column gives the scatter at this phase. The fourth column gives the phase range for which the scatter stays below 0.2 mag.

Filter	t (d)	$\sigma(M)$ (mag)	Phase range ($\sigma(M) < 0.2$ mag)	SN sample
Y	-4.4	0.15	$[-4, +1]$	CSP
J	-3.6	0.16	$[-4, +3]$	CSP
J	-3.8	0.17	$[-6, +1]$	non-CSP
H	-5.1	0.17	$[-5, +1]$	CSP
H	-4.7	0.14	$[-7, +2]$	non-CSP
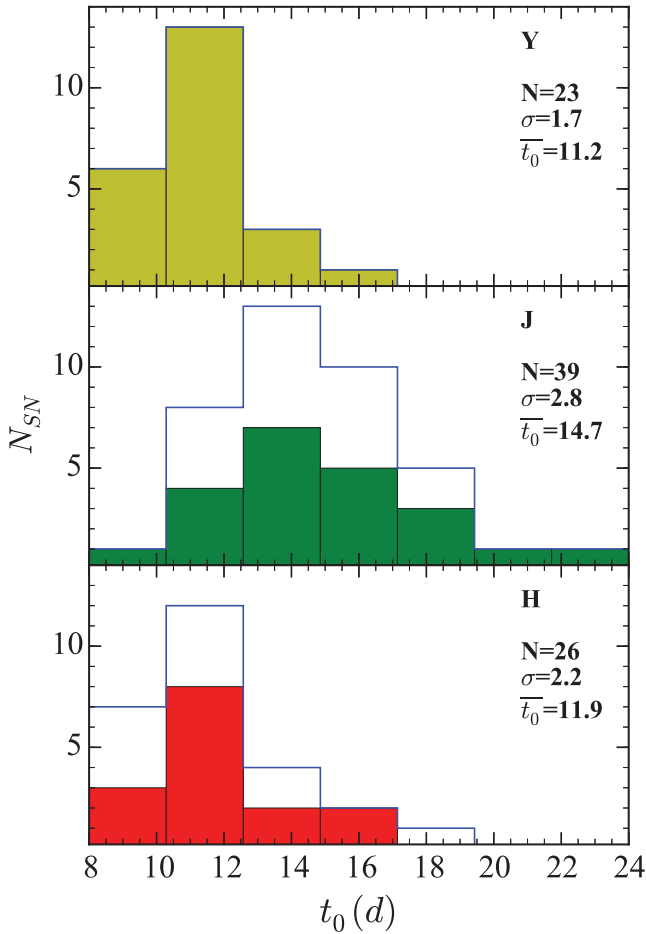
Figure 3. Distribution of t_0 in Y, J and H light curves. The Y and H minimum is reached a few days before the J light curve dips, which occurs ∼2 weeks after B-band maximum.

the second maximum. All the SNe Ia in our sample with data at these late phases comes from the CSP.

There is a tight distribution of decline rates in the Y and H bands, with the notable exception of SN 2005M in H, which declined twice as fast as the other SNe Ia. The scatter in the H-band decline rate, when excluding SN 2005M, is only 0.004 mag d^{-1}, similar to the scatter in the Y filter. The same SN is also one of the two fast declining objects in J (in the fastest bin, *middle panel*), where the scatter in the decline rates is significantly larger than for the other two bands.
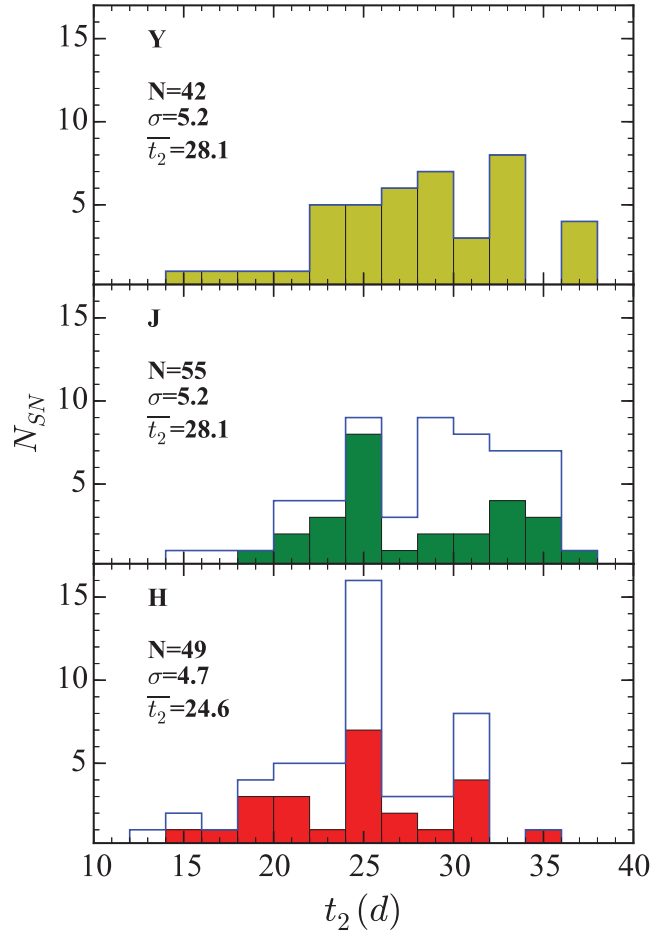
Figure 4. Distribution of t_2 in the Y, J and H light curves. Note the expanded scale on the abscissa compared to the phase ranges in Figs 2 and 3.

3.6 NIR colours

Elias et al. (1985) showed that the early $J - H$ colour evolution is rather uniform for SNe Ia. In Fig. 6, we show the colour curves ($Y - J$ and $J - H$) for the CSP and non-CSP objects. The scatter at each epoch is plotted in the lower panels. Similar to the light curves, the early colour evolution is similar for most SNe Ia in our sample.

At the first maximum, the scatter is minimal in $Y - J$ ($\sigma(Y - J) = 0.07$ mag) and in $J - H$ ($\sigma(J - H) = 0.05$ mag). The scatter stays <0.1 mag between -7 and -3 d for $Y - J$ and between -10 and -3 d for $J - H$. At early times, we find that the samples display the same scatter. Immediately after the first maximum, the colour curves start to deviate like the light curves. By the time of the minimum, the colours display a wide spread which continues to increase into the late decline.

The $Y - J$ colour remains fairly constant until about one week after maximum when the $Y - J$ colour starts a monotonic evolution towards bluer colours. For the $J - H$ colour, SNe Ia evolve to redder colours after maximum. Then after the light-curve minimum, the $J - H$ colour tends towards slightly bluer colours until ∼30 d.

4 CORRELATIONS

The uniformity of the NIR light curves at maximum light suggests that the size of the surface of last scattering at these wavelengths is independent of the details of the explosion and progenitor.
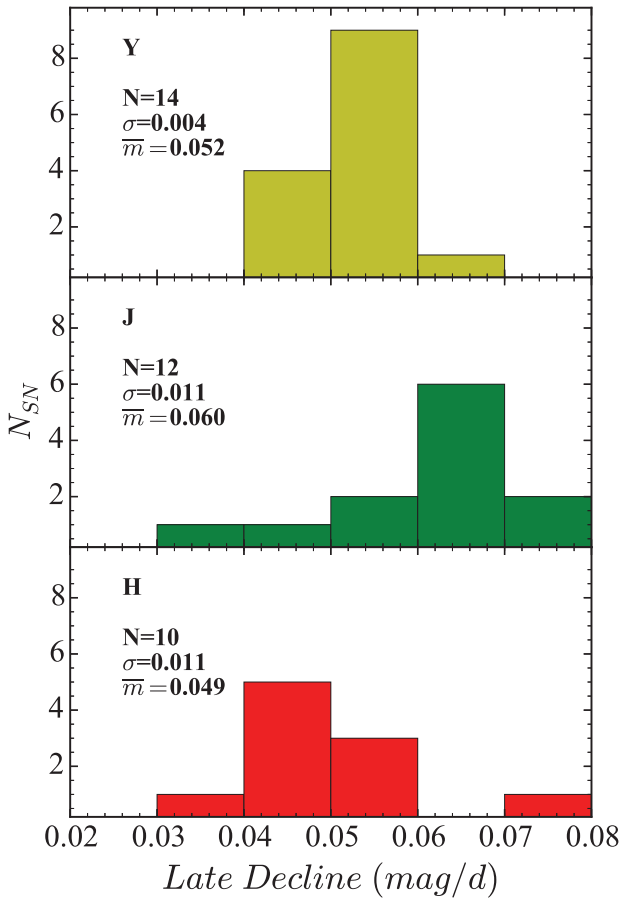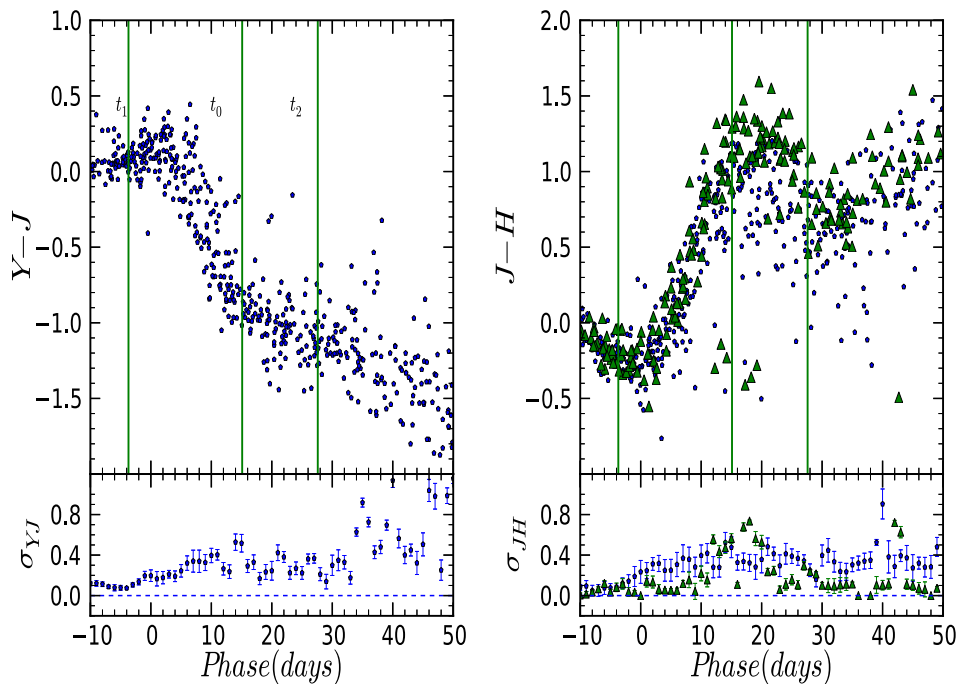
Figure 5. Distribution of decline rates after t_2.

A diversity in the NIR only becomes visible at later phases as the lines contributing to the line blanketing opacity arise from deeper in the ejecta. The phase and magnitude, the minimum and in particular the second maximum of the NIR light curves display large variations. Correlating these changes with other SN parameters should shed light on the physical processes underlying the explosions and the release of the radiation.
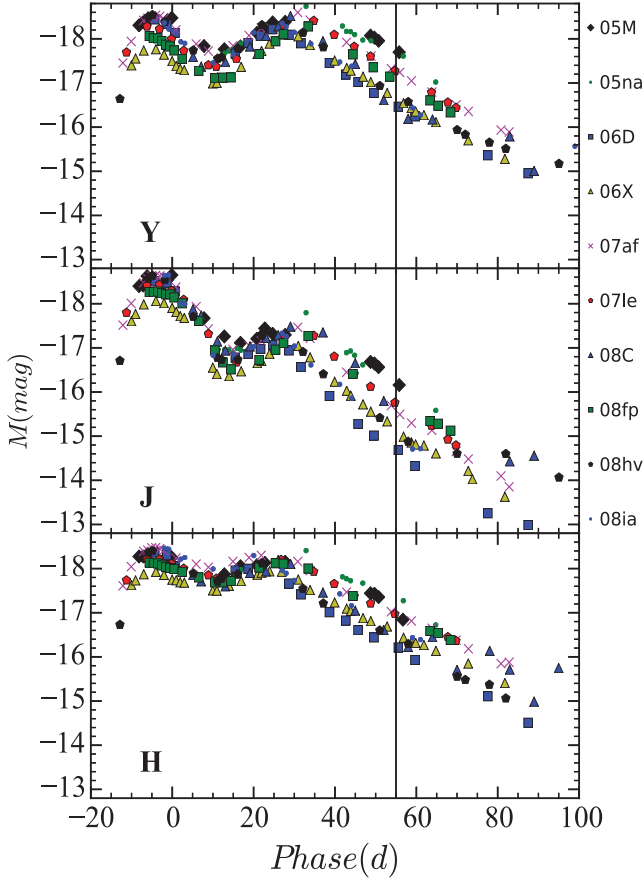
In Fig. 7, we show example NIR light curves extending to late times for 10 SNe Ia in our sample. It should be noted that among these 10 SNe are two where the extinction has been determined to be high (SN 2006X and SN 2008fp). Therefore, some of the scatter can be attributed to uncorrected host galaxy extinction.

In the following sections, we note that correlations reported with $r > 0.4$ are significant, and those with $r > 0.65$ are termed as strong.

4.1 NIR light-curve properties

In the previous section, we found a large diversity in the NIR light-curve properties at post-maximum epochs. In this section, we investigate correlations between these properties in more detail. We find a correlation between t_0 and t_2 in JH filters (Pearson parameter $r \sim 0.5$) suggesting that a later minimum is followed by a later second maximum. We also find a correlation between M_2 and M_0 in Y and J filters, with $r = 0.59$ and 0.50, respectively. This implies that SNe Ia with a more luminous minimum also display a more luminous second maximum.

Interestingly, the M_2 and t_2 do not correlate ($r < 0.4$) in any filter. However, there we do find a significant correlation across different filters between M_2 and t_2 (e.g. M_2 in the Y band correlates with t_2 in the J band with $r = 0.61$). Mandel et al. (2009) found that the rate of luminosity increase (rise rate r/β in the Mandel et al. 2009 nomenclature) to the second maximum correlated with

Figure 6. Left: $Y - J$ colour curve. The mean t_1, t_0 and t_2 in the Y filter are plotted as green lines. The scatter plot in the lower panel only contains information from the CSP objects since the non-CSP sample does not have Y-filter observations. The blue points are the objects in the CSP sample, whereas the green points are the non-CSP objects. Right: $J - H$ colour curve. The epoch of minimum scatter in J, the average value of t_0 and t_2 in J are overplotted in green. The lower panel shows the evolution of the scatter around the mean in the colour curve.

Figure 7. Complete absolute magnitude light curves in *YJH* for the 10 objects for which a late decline is measured in all three filters. The figure illustrates that the decline rates at late times are uniform, whereas there is a large scatter in the absolute magnitude at +55 d indicated by the vertical line.

the luminosity of the first peak. We cannot confirm this at any significance with our data.

Comparison of Figs 3 and 4 reveals that the light-curve evolution in the *Y* band is slowest amongst the NIR filters. SNe Ia on average reach t_0 in *Y* earlier than in *J* and *H*, but reach t_2 later in the *Y* compared to the other filters. The rise time in *Y* is nearly 4 d longer than in *J* and nearly 7 d longer than in *H*.

The phase and luminosity of the second maximum strongly correlate between the NIR filters (Fig. 8). SNe Ia with a later t_2 display a higher luminosity during the late decline. The luminosity at 55 d past the *B* maximum, hereafter referred to as $M|_{55}$ was chosen to ensure that all SNe Ia have entered the late decline well past t_2. A choice of a later phase may be more representative of the decline but would result in a smaller SN sample as not many objects are observed at these epochs and the decreasing flux results in larger uncertainties.

In Fig. 9, we plot $M|_{55}$ against t_2 and M_2. A clear trend between $M|_{55}$ and t_2 is present in all filters (Pearson coefficients *r* of 0.78, 0.92, 0.68 in the *YJH*, respectively; Fig. 9, left-hand panels). At this phase, SNe Ia are on average most luminous in *Y* followed by *H* and *J*, a trend that is already present at M_2. This is also reflected in the NIR colour evolution (see section Section 3.6).

The dispersion in $M|_{55}$ is large with $\sigma(M|_{55}) = 0.48$, 0.51 and 0.30 mag in *Y*, *J* and *H*, respectively. This is not unexpected as it
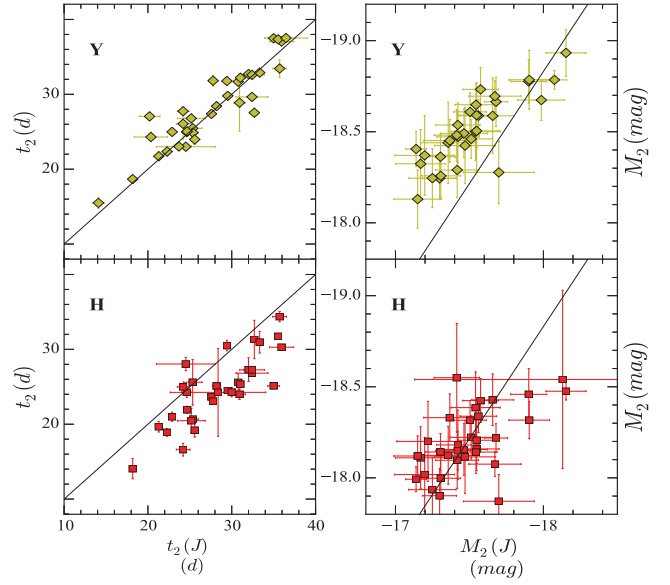
Figure 8. Phases (left) and luminosity (right) of the second maximum in NIR filters. There are clear correlations between the filters with the weakest trend in the *H* versus *J* luminosities. The black line is a one-to-one relation.
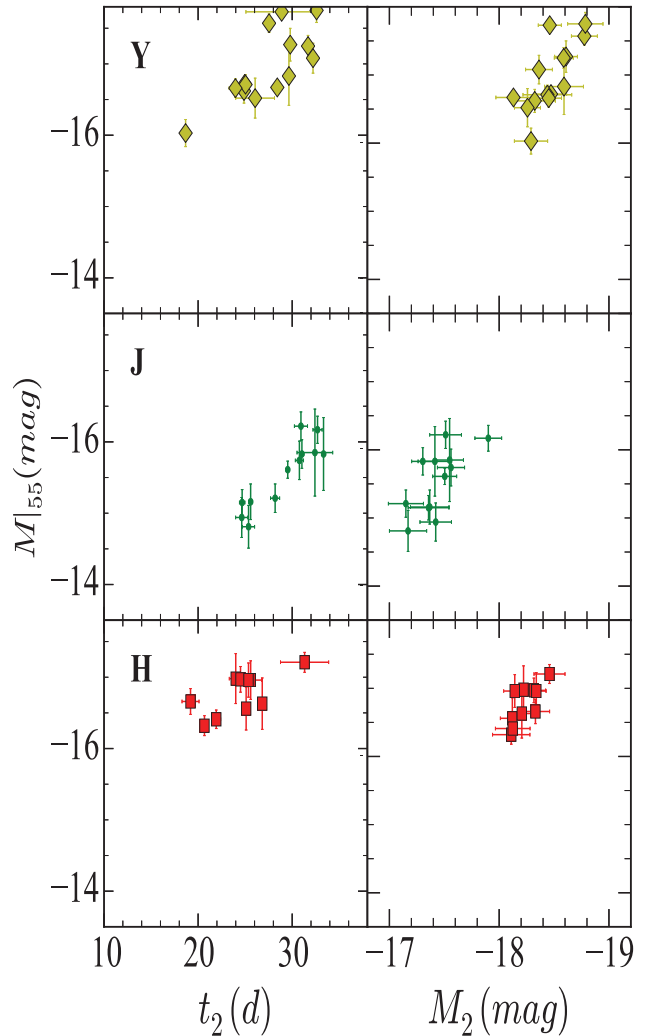
Figure 9. Left: absolute magnitude at $t = 55$ d in *YJH* versus t_2. Right: $M|_{55}$ compared to the absolute magnitude of the second maximum M_2.

continues the trend to larger (luminosity) differences in the NIR light curves with increasing phase.

4.2 Correlations with optical light-curve shape parameters

It is interesting to see whether the NIR light-curve parameters correlate with some of the well-known optical light-curve shape features (Δm_{15}; Burns et al. 2011).

Folatelli et al. (2010) have shown that the value of t_2 in i correlated with $\Delta m_{15}(B)$. Since the dispersion increases with phase, we concentrate on the second maximum and explore whether the timing and the strength correlate with the optical light-curve shape.

The second maximum in the NIR is a result of an ionization transition of the Fe-group elements from doubly to singly ionized states. Models predict that t_2 depends on the amount of Ni (M_{Ni}) synthesized in the explosion (Kasen 2006). Since M_{Ni} is known to correlate with m_B^{max}, which itself is a function of the light-curve shape (Arnett 1982; Stritzinger et al. 2006; Mazzali et al. 2007; Scalzo et al. 2014), we explored the relation between t_2 and Δm_{15} (Table 2).

Fig. 10 confirms a strong correlation between t_2 and Δm_{15}. The Pearson coefficients are 0.91, 0.93 and 0.75 for the Y, J and H bands, respectively. The weaker correlation in H may be due to a low dependence on t_2 for objects with $\Delta m_{15} < 1.2$, where t_2 appears independent of Δm_{15}. This applies only to SNe Ia with a slow optical decline. For higher Δm_{15}, the trend is as strong as in the other filters.
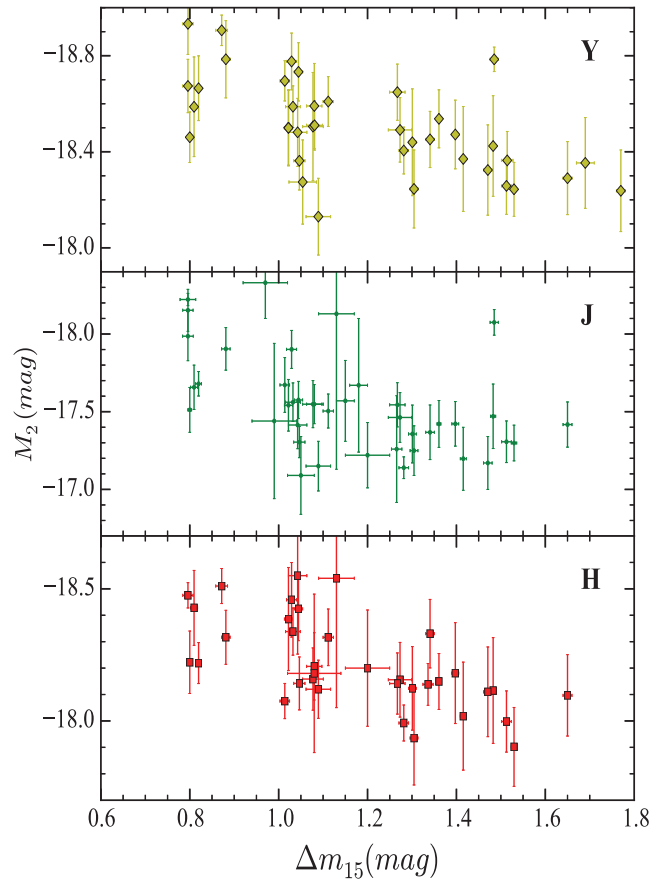

Figure 11. M_2 versus Δm_{15} is shown and a weak correlation is observed.

A linear regression yields equation (1) for each filter. The rms scatter is 2.1, 1.8 and 3.0 d in the *YJH* filters:

$$t_2(Y) = (-20.6 \pm 1.0)\Delta m_{15} + (53.6 \pm 1.2) \tag{1a}$$

$$t_2(J) = (-20.3 \pm 0.9)\Delta m_{15} + (51.7 \pm 1.1) \tag{1b}$$

$$t_2(H) = (-16.0 \pm 2.7)\Delta m_{15} + (42.3 \pm 2.8). \tag{1c}$$

Since the phase of the second maximum (t_2) in NIR bands is strongly correlated with Δm_{15} and thereby the optical maximum luminosity, t_2 could also serve as an indicator of the luminosity of SNe Ia. It is noteworthy that even extreme cases, like SN 2007if, which have been associated with super-Chandrasekhar mass progenitors (Scalzo et al. 2010, 2012) are fully consistent with the derived relations.

There is a weak correlation between M_2 and Δm_{15} as shown in Fig. 11, with very little difference between objects. We find r values of 0.59, 0.50 and 0.63 for the Y, J and H filters, respectively.

5 DISCUSSION

As has been shown earlier in this paper and in a number of other publications (Meikle 2000; Wood-Vasey et al. 2008; Barone-Nugent et al. 2012; Weyant et al. 2014), SN Ia NIR light curves show remarkable uniformity around maximum light, compared to that at optical wavelengths. This uniformity, combined with reduced effects of extinction, holds great promise for the use of SNe Ia as distance indicators in the NIR. Kattner et al. (2012) proposed to further reduce the scatter in the luminosity of the first maximum in

Figure 10. Comparison of t_2 in the NIR light curves with $\Delta m_{15}(B)$.

the NIR by a decline rate correction similar to the procedure in the optical.

The spread in optical luminosity is attributed to different masses, or distributions, of ^{56}Ni within the ejecta (Arnett 1982; Stritzinger et al. 2006; Scalzo et al. 2014). The indifference of the NIR maximum light to the nickel mass suggests that it is intermediate-mass elements that dominate the opacity in these bands at maximum light.

The NIR light curves showed an increased dispersion at later times. We attribute this increased scatter to differences in the speed of the evolution of the SNe Ia. The phase of the second maximum depends on the mass and distribution of ^{56}Ni, the change in opacity, the ionization and the dominant species setting the emission.

Not all SNe Ia display a second maximum (e.g. Krisciunas et al. 2009), and we restricted our analysis only to objects in which the second maximum is defined well enough to be fitted. This translates into a sample including only SNe Ia with $\Delta m_{15}(B) < 1.8$ mag. Events without a second maximum tend to be of low luminosity, often similar to SN 1991bg, and with large $\Delta m_{15}(B)$.

The strength of the second peak in the $iJHK$ light curves does not correlate with Δm_{15}, but the phase does (Folatelli et al. 2010; Biscardi et al. 2012).

As presented in the previous section, we confirm this relation between t_2 and Δm_{15} for the YJH filters. The correlation of M_2 with Δm_{15} is rather weak (Fig. 11), although it appears somewhat stronger than in Biscardi et al. (2012) (the Pearson coefficients in our data are 0.5 and 0.63 for J and H compared to 0.12 and 0.08 in Biscardi et al. 2012).

5.1 A possible physical picture

The various features of the NIR light curves can be assembled into a physical picture of the explosions. The striking similarities of the late-decline rates, when the SN becomes increasingly transparent to the γ-rays generated by the radioactive decays, indicate that the internal structure of the explosions is probably similar for all SNe Ia considered here. The uniform decline rates are consistent with the predictions of Woosley et al. (2007) for a range of Chandrasekhar-mass models, with different M_{Ni} but similar radial distribution of iron-group elements. We find that the late-time decline rate in J is faster than in Y and H, a trend also seen between the simulated J and H light curves in Dessart et al. (2014). The NIR light curves depend very little on the explosion geometry (Kromer & Sim 2009). The DDC15 models of Blondin et al. (2013) show that the YHK decline rates are similar to the pseudo-bolometric decline rate (Blondin, private communication). The J band shows a faster decline due to a lack of emission features (Spyromilio et al. 1994). This also explains the evolution of the $J - H$ colour curve to redder colours at late times.

At the these late times, $M|_{55}$ shows a large scatter (cf. Fig. 9). If the similar late-decline rates(cf. Fig. 5) indicate a similarity in the evolution of the γ-ray escape fraction for different SNe Ia, then a higher luminosity would translate into a higher energy input at late phases, i.e. a larger mass of Fe-group elements.

Kasen (2006) predicted that the second maximum should be delayed for larger Fe masses, which is exactly what is observed in the NIR (see also Jack, Hauschildt & Baron 2012). According to Kasen & Woosley (2007), the faster decline in the B-band light curve is mostly due to line blanketing through Fe and Co lines, which shifts the emission into the NIR and shapes the NIR light curves after maximum. The optical colour evolution post-B-maximum is suggested to be more rapid for explosions with lower Ni masses. If this is true, then the onset of the uniform $B - V$ colour evolution (referred to as
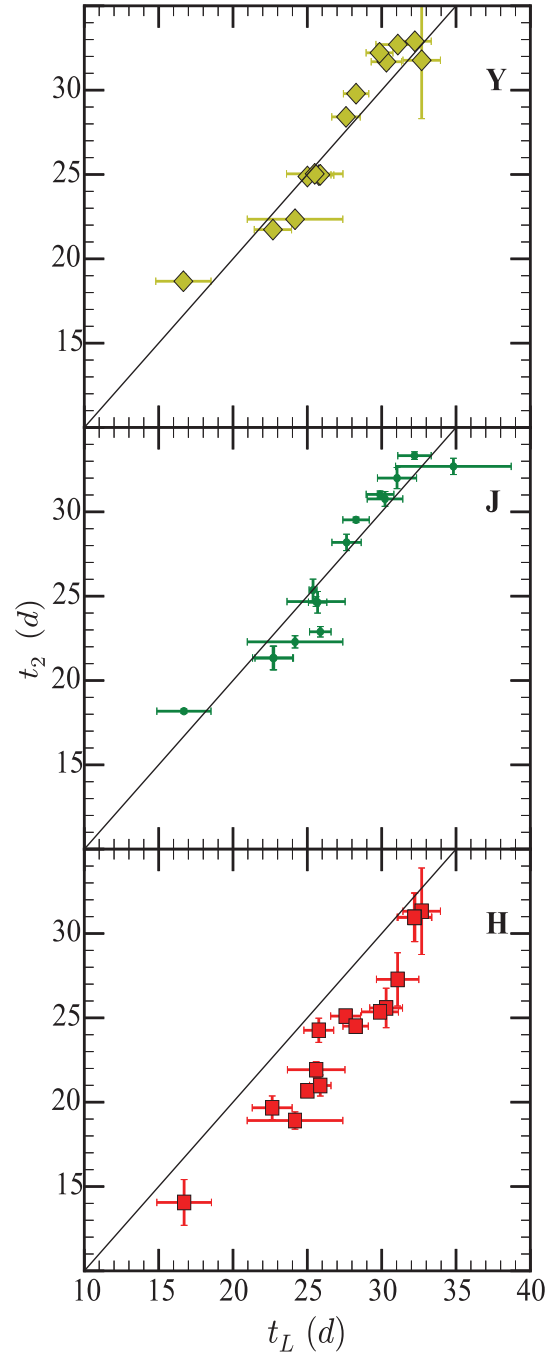
Figure 12. The phase of the second maximum versus t_L. The black line is the one-to-one relation.

the 'Lira law' and originally defined as the uniformity of the slope of the colour curve from 30 to 90 d, although the onset is generally at earlier phase; Phillips et al. 1999) marks the beginning of the nebular phase. At these epochs, the SN Ia spectrum is dominated by emission lines from Fe-group elements and the emission line strength depends on the Fe mass in the explosion. We measure the time at which the SN enters the Lira law, hereafter t_L, as the epoch of inflection in the $(B - V)$ colour curve, at late times. The procedure for measuring t_L is identical to the measurement of t_2 described in Section 3.4.

Fig. 12 shows that t_2 coincides nearly exactly with t_L for the Y and J bands. While the H light curve peaks 3–4 d earlier. The reason
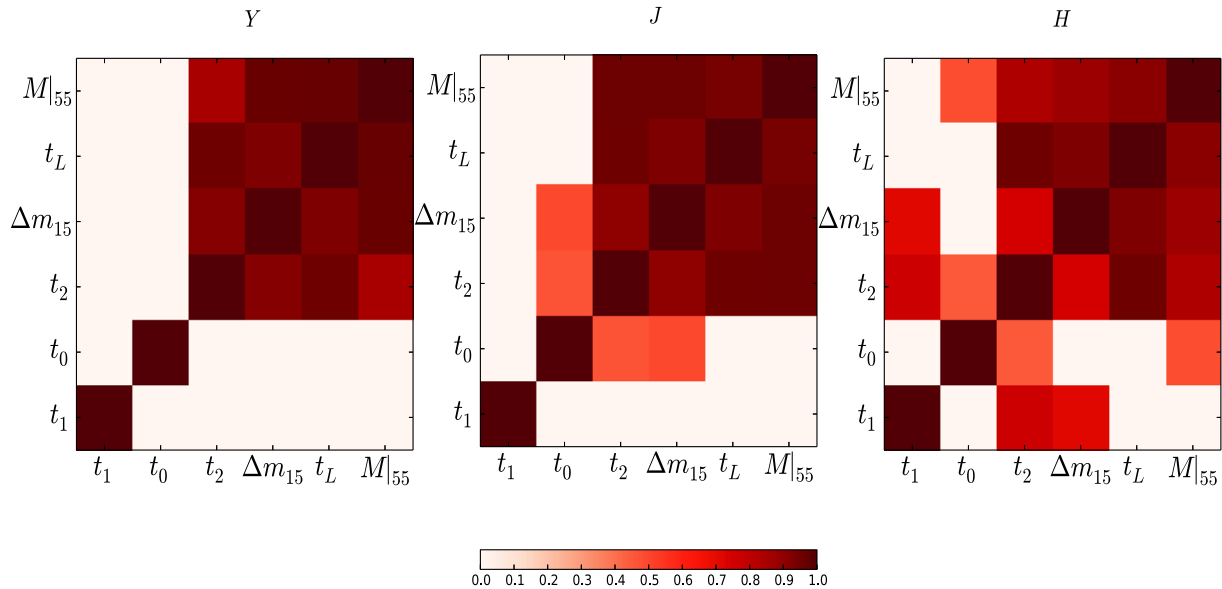
Figure 13. A summary of the correlations between the timing parameters (t_1, t_0 and t_2), Δm_{15}, t_L and the late-time luminosity ($M|_{55}$), in each filter. There is a strong correlation amongst the t_2, Δm_{15}, t_L and $M|_{55}$ ($r > 0.65$). The colour bar scales from white to red in ascending order of correlation strength. Correlations with $r < 0.4$ have been set to white.

for this is not entirely clear, but both the Y and J bands are expected to be strongly influenced by Fe lines, while H is dominated by Co lines (e.g. Marion et al. 2009; Jack et al. 2012). The striking coincidence of t_2 and t_L in the NIR light curves is further evidenced that t_2 directly depends on the Ni mass in the explosion.

Scalzo et al. (2014) found that the Ni mass depends on $\Delta m_{15}(B)$ and the bolometric peak luminosity. All these parameters ($m_B^{\max}$, $\Delta m_{15}(B)$, t_2 and t_L and NIR late-phase luminosity) can be tied to the Ni (and/or Fe) mass in the explosion. We provide a summary of the important correlations analysed in this work for the three NIR filters in Fig. 13, where we correlate the timing parameters (t_1, t_0, t_2), Δm_{15}, t_L and NIR late-phase luminosity ($M|_{55}$). With most of the Fe synthesized in the explosion, we propose that all light-curve parameters point to the Ni as the dominant factor in shaping the light curves. We find a consistent picture that the properties of second maximum in the NIR light curves are strongly influenced by the amount of Ni produced in the explosion followed by a more luminous decline.

The NIR colours show a pronounced evolution after t_1, the flux in the J band decreases significantly with respect to both Y and H shortly after t_1 (Fig. 6). The reason for this depression is most likely the lack of transitions providing the required channel for radiation to emerge around 1.2 μm (Spyromilio et al. 1994; Höflich, Khokhlov & Wheeler 1995; Wheeler et al. 1998). This persists until t_2 when the [Fe II] (1.25 μm) emission line forms and the J-band magnitude recovers relative to H, although not compared with Y, which is also dominated by Fe lines (Marion et al. 2009). The H filter is dominated by Co II lines (e.g. Kasen 2006; Jack et al. 2012). After the second maximum, $J - H$ turns redder again due to the faster decline rate in the J filter.

We investigated whether the (optically) fast-declining SNe Ia can be grouped within our analysis. These SNe have very low ^{56}Ni mass which is almost certainly centrally located (low velocities of Fe III in the optical at late times in SN 1991bg; Mazzali et al. 1998) and transition so rapidly that a second maximum barely has time to form. Thus, we could not include them directly in our study. However, a

comparison of $M|_{55}$ with $\Delta m_{15}(B)$ can be made for four objects of this class (SNe 2005ke, 2006mr, 2007N and 2007ax). The trend of these objects showing a fainter $M|_{55}$ luminosity with larger $\Delta m_{15}(B)$ is followed, but it is unclear whether these SN 1991bg-like SNe Ia follow the same relation as their brighter counterparts. The result remains inconclusive as the scatter remains currently too large. We note that the decline rates in the NIR at late times for these objects do not differ significantly from our sample. They follow the same distribution as in Fig 5.

5.2 Improved distance measurements?

The uniformity of the NIR light curves is in use for cosmological projects (Barone-Nugent et al. 2012; Weyant et al. 2014). Krisciunas et al. (2009) finds no correlation of the maximum luminosity with other light-curve parameters, but identified the (optically) fast-declining SNe Ia as subluminous in the NIR compared to the other SNe Ia in their sample. In Kattner et al. (2012), the authors find a weak trend between the NIR first maximum luminosity and Δm_{15}.

We looked for NIR light-curve properties to further improve SNe Ia as distance indicators. In Fig. 14, we find no significant evidence for a correlation between M_1 and t_2 for objects in our sample. The faintness of SN 2006X in this diagram is probably due to the strong absorption towards this SN.

The scatter in Fig. 1 falls to around 0.2 mag at later NIR phases. Between t_0 and t_2 all NIR light curves reach comparable luminosities. These phases are between 10 and 20 d in Y, near 15 and 20 d in J and H when SNe Ia are only about 1 (0.5) mag fainter than at the first maximum in Y (H). The decline in the J light curves is quite steep after the first maximum and the SNe have already faded by nearly 2 mag. At least for Y and H, it might be worthwhile to investigate whether good distances can be determined at later phases (between +10 and +15 d). The advantage would be a distance measurement with a reduced extinction component, i.e. mostly independent of the exact reddening law, and the possibility
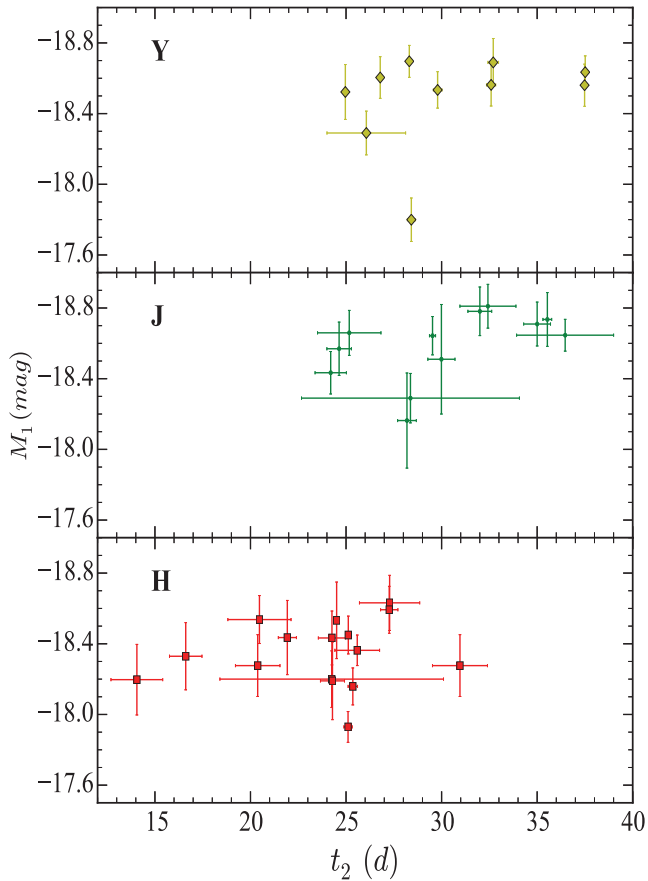
Figure 14. The magnitude of the first maximum in the *YJH* bands is plotted against the phase of the second maximum in the *J* band. The underluminous object in the *Y* and *J* bands is the heavily extinguished SN 2006X. In the *J* band, SN 2014J also appears fainter.

of targeted NIR observations even when the first maximum had been missed.

6 CONCLUSIONS

The cosmological interest in SNe Ia in the NIR stems from the small observed scatter in the peak magnitudes. We confirm this with our extended literature sample despite our simple assumptions on distances and neglect of host galaxy absorption. The phase of the first maximum in the *YJH* light curves shows a narrow distribution. The uniformity of the SNe Ia in the NIR lasts until about one week past *B* maximum. The NIR light curves diverge showing a large scatter by the time of the second maximum and thereafter. The IR colour curves are uniform at early phases with increasing scatter after 20 d.

These findings corroborate the use of only few IR observations near the first maximum to obtain good cosmological distances (Barone-Nugent et al. 2012; Weyant et al. 2014). The small scatter prevails for nearly a week around the first maximum and potentially another window opens near the second maximum, where the scatter again appears rather small. A condition for these measurements is accurate phase information to be able to use sparse NIR observations to derive the distances. The phase information could come from accurate optical light curves, as used here, or through

spectra. The latter are needed for redshifts and classification in any case.

The information contained in the NIR light curves points towards the nickel/iron mass as the reason for the variations. The absolute magnitude 55 d past maximum together with the very uniform decline rate of the light curves in all bands, including the optical (Barbon, Ciatti & Rosino 1973; Phillips et al. 1999; Leibundgut 2000), points towards differences of the energy input into the ejecta with a rather uniform density structure. This is also found in theoretical studies (Kasen & Woosley 2007; Kromer & Sim 2009; Dessart et al. 2014), although most of these models employ Chandrasekhar-mass explosions and a wider range of ejecta mass models may need to be explored to confirm the similarities in the structure of the ejecta. A higher luminosity at a fixed phase in the nebular phase points towards a larger iron core and hence a higher nickel production in the explosion. A corollary is the phase of the second maximum which also occurs later for larger iron cores (Kasen 2006).

The strong correlation of the phase of the second IR maximum with the optical light-curve shape parameter Δm_{15} and the onset of the uniform $(B - V)$ colour evolution ('Lira law') point towards SNe Ia as an ordered family and nickel mass as the dominating factor in shaping the appearance of SNe Ia. With a higher nickel mass, a larger Fe core is expected. This would result in higher expansion velocities observed at late phases (Mazzali et al. 1998). It is worth checking whether this prediction holds true in future observations.

The phase of the second maximum should provide a handle to determining the nickel masses in SN Ia explosions, in particular for SNe Ia where absorption is significant. In cases like SN 2014J, the NIR light curve can yield an independent check on the nickel mass and a direct comparison to the direct measurements of the γ-rays from the nickel decay (Churazov et al. 2014; Diehl et al. 2014). A calibration of a fair set of (preferably bolometric) peak luminosities and the derived nickel masses with our parameter t_2 should lead to the corresponding relation.

We attempted to improve the IR first maximum for distance measurements and looked for a possible correlation of M_1 with the phase of the second maximum. There is a slight improvement in the *J* band and none in *Y* and *H*. The resulting scatter after correction in the *J* band is 0.16 mag. This is comparable to the observed value from previous studies (Mandel et al. 2009; Kattner et al. 2012; Weyant et al. 2014). It remains to be seen whether larger samples will provide a better handle in the future.

Since we specifically studied the second maximum in the NIR light curves, we excluded SNe Ia, which do not display this feature. These are objects similar to either SN 1991bg, SN 2000cx or SN 2002cx and are typically faint and peculiar SNe (Filippenko et al. 1992; Leibundgut et al. 1993; Li et al. 2001, 2003; Foley et al. 2013). They appear to also display a fainter first maximum in the NIR (Krisciunas et al. 2009). It would be interesting to check whether the uniform decline rate observed in the NIR also applies to SNe Ia which do not show the second maximum. This could be used to check whether these explosions share some physical characteristics with the ones discussed here. There are only very few SNe Ia of this type and we do not find a conclusive answer. Increasing the number of SNe Ia with this information is important to assess the physical differences among the different SN Ia groups. The recent CFAIR2 catalogue (Friedman et al. 2014) will provide some of these data.

The NIR light curves display a decline rate after the second maximum, which is significantly larger than the optical light curves

at the same phase (e.g. Leibundgut 2000). At very late phases ($\geq$200 d), the NIR light curves become nearly flat as observed for SN 2001el, while there is no observable change in the optical decline rates (Stritzinger & Sollerman 2007). It would be interesting to observe the change in decline rate between 100 and 300 d. Presumably, the internal structure of the explosions sets the transition towards the positron decays as the dominant energy source, when the ejecta have thinned enough that the γ-rays escape freely. This phase might be correlated with other physical parameters, like the nickel and ejecta mass, determined through early light curves.

A possible extension of this photometric study with detailed spectroscopic observations and theoretical spectral synthesis calculations might be worthwhile to check on the emergence of the various emission lines, trace the exact transition to the flatter IR light curves and determine whether it indicates any differences in the structure of the SNe, e.g. transition to positron channel.

Finally, Euclid will discover many SNe at NIR wavelengths out to cosmologically interesting redshifts (e.g. Astier et al. 2014). With the small scatter of the peak luminosity, these observations will provide distances with largely reduced uncertainties due to reddening. Our study confirms the promise the NIR observations of SNe Ia offer.

REFERENCES

Ajhar E. A., Tonry J. L., Blakeslee J. P., Riess A. G., Schmidt B. P., 2001, ApJ, 559, 584
Amanullah R. et al., 2014, ApJ, 788, 21
Arnett W. D., 1982, ApJ, 253, 785
Astier P. et al., 2014, A&A, 572, A80
Barbon R., Ciatti F., Rosino L., 1973, A&A, 25, 241
Barone-Nugent R. L. et al., 2012, MNRAS, 425, 1007
Benetti S. et al., 2004, MNRAS, 348, 261
Biscardi I. et al., 2012, A&A, 537, A57
Blondin S., Dessart L., Hillier D. J., Khokhlov A. M., 2013, MNRAS, 429, 2127
Burns C. R. et al., 2011, AJ, 141, 19
Burns C. R. et al., 2014, ApJ, 789, 32
Cardelli J. A., Clayton G. C., Mathis J. S., 1989, ApJ, 345, 245
Cartier R. et al., 2014, ApJ, 789, 89
Churazov E. et al., 2014, Nature, 512, 406
Conley A. et al., 2011, ApJS, 192, 1
Contardo G., Leibundgut B., Vacca W. D., 2000, A&A, 359, 876
Contreras C. et al., 2010, AJ, 139, 519
Dessart L., Hillier D. J., Blondin S., Khokhlov A., 2014, MNRAS, 441, 3249
Diehl R. et al., 2014, A&A, preprint (arXiv:1409.5477)
Elias J. H., Frogel J. A., Hackwell J. A., Persson S. E., 1981, ApJ, 251, L13
Elias J. H., Matthews K., Neugebauer G., Persson S. E., 1985, ApJ, 296, 379
Elias-Rosa N. et al., 2006, MNRAS, 369, 1880
Filippenko A. V. et al., 1992, AJ, 104, 1543
Folatelli G. et al., 2010, AJ, 139, 120
Foley R. J. et al., 2013, ApJ, 767, 57
Foley R. J. et al., 2014, MNRAS, 443, 2887
Freedman W. L. et al., 2001, ApJ, 553, 47
Freedman W. L. et al., 2009, ApJ, 704, 1036
Friedman A. S. et al., 2014, preprint (arXiv:1408.0465)
Goobar A., Leibundgut B., 2011, Annu. Rev. Nucl. Part. Sci., 61, 251
Guy J., Astier P., Nobili S., Regnault N., Pain R., 2005, A&A, 443, 781
Guy J. et al., 2007, A&A, 466, 11
Guy J. et al., 2010, A&A, 523, A7
Hamuy M., Phillips M. M., Suntzeff N. B., Schommer R. A., Maza J., Smith R. C., Lira P., Aviles R., 1996, AJ, 112, 2438
Höflich P., Khokhlov A., Wheeler C., 1995, Haas M. R., Davidson J. A., Erickson E. F., eds, ASP Conf. Ser., Vol. 73, Airborne Astronomy Symposium on the Galactic Ecosystem: From Gas to Stars to Dust. Astron. Soc. Pac., San Francisco, p. 441
Jack D., Hauschildt P. H., Baron E., 2012, A&A, 538, A132
Jensen J. B., Tonry J. L., Barris B. J., Thompson R. I., Liu M. C., Rieke M. J., Ajhar E. A., Blakeslee J. P., 2003, ApJ, 583, 712
Jha S., Riess A. G., Kirshner R. P., 2007, ApJ, 659, 122
Kasen D., 2006, ApJ, 649, 939
Kasen D., Woosley S. E., 2007, ApJ, 656, 661
Kattner S. et al., 2012, PASP, 124, 114
Krisciunas K. et al., 2003, AJ, 125, 166
Krisciunas K. et al., 2004a, AJ, 127, 1664
Krisciunas K. et al., 2004b, AJ, 128, 3034
Krisciunas K. et al., 2007, AJ, 133, 58
Krisciunas K. et al., 2009, AJ, 138, 1584
Kromer M., Sim S. A., 2009, MNRAS, 398, 1809
Leaman J., Li W., Chornock R., Filippenko A. V., 2011, MNRAS, 412, 1419
Leibundgut B., 1988, PhD thesis, Univ. Basel
Leibundgut B., 2000, A&AR, 10, 179
Leibundgut B. et al., 1993, AJ, 105, 301
Leloudas G. et al., 2009, A&A, 505, 265
Li W. et al., 2001, PASP, 113, 1178
Li W. et al., 2003, PASP, 115, 453
Mandel K. S., Wood-Vasey W. M., Friedman A. S., Kirshner R. P., 2009, ApJ, 704, 629
Marion G. H., Höflich P., Gerardy C. L., Vacca W. D., Wheeler J. C., Robinson E. L., 2009, AJ, 138, 727
Matheson T. et al., 2012, ApJ, 754, 19
Mazzali P. A., Chugai N., Turatto M., Lucy L. B., Danziger I. J., Cappellaro E., della Valle M., Benetti S., 1997, MNRAS, 284, 151
Mazzali P. A., Cappellaro E., Danziger I. J., Turatto M., Benetti S., 1998, ApJ, 499, L49
Mazzali P. A., Röpke F. K., Benetti S., Hillebrandt W., 2007, Science, 315, 825
Meikle W. P. S., 2000, MNRAS, 314, 782
Nobili S. et al., 2005, A&A, 437, 789
Pastorello A. et al., 2007, MNRAS, 377, 1531
Peacock J. A., Schneider P., Efstathiou G., Ellis J. R., Leibundgut B., Lilly S. J., Mellier Y., 2006, ESA and ESO, Report on the ESA-ESO Working Group on Fundamental Cosmology, preprint (arXiv:astro-ph/0610906)
Perlmutter S. et al., 1999, ApJ, 517, 565
Phillips M. M., 1993, ApJ, 413, L105

Phillips M. M., 2012, PASA, 29, 434

Phillips M. M., Lira P., Suntzeff N. B., Schommer R. A., Hamuy M., Maza
    J., 1999, AJ, 118, 1766

Phillips M. M. et al., 2006, AJ, 131, 2615

Phillips M. M. et al., 2013, ApJ, 779, 38

Pignata G. et al., 2008, MNRAS, 388, 971

Riess A. G., Press W. H., Kirshner R. P., 1996, ApJ, 473, 88

Riess A. G. et al., 1998, AJ, 116, 1009

Scalzo R. et al., 2010, ApJ, 713, 1073

Scalzo R. et al., 2012, ApJ, 757, 12

Scalzo R. et al., 2014, MNRAS, 560

Scolnic D. M., Riess A. G., Foley R. J., Rest A., Rodney S. A., Brout D. J.,
    Jones D. O., 2014, ApJ, 780, 37

Spyromilio J., Pinto P. A., Eastman R. G., 1994, MNRAS, 266, L17

Stritzinger M., Sollerman J., 2007, A&A, 470, L1

Stritzinger M., Leibundgut B., Walch S., Contardo G., 2006, A&A, 450, 241

Stritzinger M. D. et al., 2011, AJ, 142, 156

Tonry J. L., Dressler A., Blakeslee J. P., Ajhar E. A., Fletcher A. B., Luppino
    G. A., Metzger M. R., Moore C. B., 2001, ApJ, 546, 681

Tully R. B., 1988, Nearby Galaxies Catalog. Cambridge Univ. Press,
    Cambridge

Valentini G. et al., 2003, ApJ, 595, 779

Weyant A., Wood-Vasey W. M., Allen L., Garnavich P. M., Jha S. W., Joyce
    R., Matheson T., 2014, ApJ, 784, 105

Wheeler J. C., Höflich P., Harkness R. P., Spyromilio J., 1998, ApJ, 496,
    908

Willick J. A., Courteau S., Faber S. M., Burstein D., Dekel A., Strauss
    M. A., 1997, ApJS, 109, 333

Wood-Vasey W. M. et al., 2008, ApJ, 689, 377

Woosley S. E., Kasen D., Blinnikov S., Sorokina E., 2007, ApJ, 662, 487

APPENDIX A: PARAMETER TABLES FOR THE CORRELATIONS

Table A2. *J* filter apparent magnitude and phase of the two maxima and the minimum for the complete sample. The phases are given in days relative to the *B* maximum. The full table is available online.

SN	t_1 (d)	m_1	t_0 (d)	m_0	t_2 (d)	m_2
1980N	–	–	–	–	21.86 ± 2.70	–
1981B	–	–	–	–	32.19 ± 0.10	–
1986G	–	–	–	–	16.40 ± 1.40	–
1998bu	–	–	–	–	29.84 ± 0.40	–
1999ac	–	–	–	–	27.00 ± 2.00	15.61 ± 0.50

Table A3. *H* filter apparent magnitudes and phases of the two maxima and the minimum for the complete sample. The phases are given in days relative to the *B* maximum. The full table is available online.

SN	t_1 (d)	m_1	t_0 (d)	m_0	t_2 (d)	m_2
1981B	...	–	–	–	31.98 ± 0.50	–
1986G	–	–	–	–	12.70 ± 1.30	10.01 ± 0.10
1998bu	–	–	–	–	29.18 ± 1.65	–
1999ee	–	–	–	–	30.50 ± 0.70	15.11 ± 0.03
2000E	–	–	–	–	25.10 ± 0.70	13.85 ± 0.10

Table A4. Late-time decline rate and luminosity at +55 d in *YJH*. The full table is available online.

SN	slope (mag/d)	err	$M\vert_{55}$	err
Y filter				
2005M	0.054	0.002	-17.73	0.08
2005el	0.056	0.002	-16.72	0.11
2005na	0.052	0.003	-17.57	0.13
2006D	0.050	0.001	-16.62	0.17
2006X	0.054	0.003	-16.67	0.10

Table A1. *Y* filter apparent magnitude and phase of the two maxima and the minimum for the complete sample. The phases are given in days relative to the *B* maximum. The full table is available online.

SN	t_1 (d)	m_1	t_0 (d)	m_0	t_2 (d)	m_2
2004eo	-4.48 ± 0.82	15.90 ± 0.03	–	–	–	–
2004ey	–	–	–	–	31.77 ± 0.20	15.51 ± 0.01
2004gs	–	–	8.10 ± 0.76	17.69 ± 0.02	22.35 ± 0.07	17.16 ± 0.03
2004gu	–	–	–	–	37.04 ± 0.13	17.67 ± 0.03
2005A	–	–	13.70 ± 1.61	17.69 ± 0.41	27.39 ± 0.07	16.00 ± 0.11

Table A5. t_2 and epoch at which SN enters Lira law. The full table is available online.

SN	t_2 (d)	err	t_L (d)	err
Y filter				
2004gs	22.34	0.07	24.17	3.21
2005am	21.73	0.12	22.69	1.26
2005el	24.96	0.11	25.78	1.00
2005na	31.77	3.46	32.69	1.26
2006D	24.88	0.02	25.00	0.26

SUPPORTING INFORMATION

Additional Supporting Information may be found in the online version of this article:

Table A1. *Y* filter apparent magnitude and phase of the two maxima and the minimum for the complete sample.

Table A2. *J* filter apparent magnitude and phase of the two maxima and the minimum for the complete sample.
Table A3. *H* filter apparent magnitudes and phases of the two maxima and the minimum for the complete sample.
Table A4. Late-time decline rate and luminosity at +55 d in *YJH*.
Table A5. t_2 and epoch at which SN enters Lira law.
(http://mnras.oxfordjournals.org/lookup/suppl/doi:10.1093/mnras/stu2716/-/DC1).

Please note: Oxford University Press is not responsible for the content or functionality of any supporting materials supplied by the authors. Any queries (other than missing material) should be directed to the corresponding author for the article.

This paper has been typeset from a TEX/LATEX file prepared by the author.